

A major purpose of the Technical Information Center is to provide the broadest dissemination possible of information contained in DOE's Research and Development Reports to business, industry, the academic community, and federal, state and local governments.

Although a small portion of this report is not reproducible, it is being made available to expedite the availability of information on the research discussed herein.

CONF

PORTIONS OF THIS REPORT ARE ILLEGIBLE. It
has been reproduced from the best available
copy to permit the broadest possible avail-
ability.

Los Alamos National Laboratory is operated by the University of California for the United States Department of Energy under contract W-7405-ENG-36

LA-UR--84-1649

TITLE HYDROGEN TRANSPORT, MIXING, AND COMBUSTION STUDIES

DE84 012455

AUTHOR(S) J. R. Travis

SUBMITTED TO IAEA Technical Committee/Workshop on the Uses of Computer Codes
for Nuclear Reactor Safety Analysis, Varna, Bulgaria, 28 May -
1 June 1984.

DISCLAIMER

This report was prepared as an account of work sponsored by an agency of the United States Government. Neither the United States Government nor any agency thereof, nor any of their employees, makes any warranty, express or implied, or assumes any legal liability or responsibility for the accuracy, completeness, or usefulness of any information, apparatus, product, or process disclosed, or represents that its use would not infringe privately owned rights. Reference herein to any specific commercial product, process, or service by trade name, trademark, manufacturer, or otherwise does not necessarily constitute or imply its endorsement, recommendation, or favoring by the United States Government or any agency thereof. The views and opinions of authors expressed herein do not necessarily state or reflect those of the United States Government or any agency thereof.

By acceptance of this article the publisher recognizes that the U.S. Government retains a nonexclusive, royalty-free license to publish or reproduce the published form of this contribution, or to allow others to do so for U.S. Government purposes. The Los Alamos National Laboratory requests that the publisher identify this article as work performed under the auspices of the U.S. Department of Energy.

Los Alamos Los Alamos National Laboratory
Los Alamos, New Mexico 87545

2

HYDROGEN TRANSPORT, MIXING, AND COMBUSTION STUDIES

J. R. Travis

Theoretical Division, Group T-3
University of California
Los Alamos National Laboratory
Los Alamos, New Mexico 87545

ABSTRACT

The transport, mixing, and burning of hydrogen inside containments is receiving a great deal of attention. We present very detailed models describing this important phenomena and provide several example calculations to show the versatility and accuracy of the methods.

I. INTRODUCTION

During and after a loss-of-coolant accident in a light-water reactor, water may be decomposed by chemical reactions and radiolysis to release gaseous hydrogen. Under these conditions, hydrogen may be released into the reactor containment resulting in two deleterious effects: (1) the noncondensable gas can increase containment pressure, and (2) in sufficient amounts, the hydrogen could burn in the presence of air and cause considerable loads on the containment walls and crucial control devices. Each effect represents an additional safety risk.

To better assess the problem, we have adapted an existing two-dimensional combustion code CONCHAS-SPRAY [1] to analyze hydrogen combustion, and we have developed a three-dimensional code HMS [2,3] to calculate the details of hydrogen transport through containment structures and extended it's capabilities (HMS-Burn [4,5]) to include combustion.

Several examples are offered to demonstrate the capability of hydrogen mixing and combustion through containments.

II. MATHEMATICAL MODEL

The partial-differential equations that govern the fluid dynamics and species transport and model the hydrogen combustion process are presented in this section.

The Mixture Equations

The mixture mass conservation equation is

$$\frac{\partial \rho}{\partial t} + \nabla \cdot (\rho \bar{u}) = 0 \quad ,$$

where

$$\rho = \sum_{a=1}^4 \rho_a \quad ; \quad \rho_a = \text{macroscopic density of the individual species (H}_2\text{O, N}_2, \text{H}_2 \text{ or O}_2\text{)},$$

$$\bar{u} = \text{mass-average velocity vector.}$$

The mixture-momentum conservation equations are given by

$$\frac{\partial (\rho \bar{u})}{\partial t} + \nabla \cdot (\rho \bar{u} \bar{u}) = - \nabla p + \nabla \cdot \bar{\sigma} + \rho \bar{g} - \bar{D} \quad ,$$

where

p = pressure,

$\bar{\sigma}$ = viscous stress tensor,

\bar{n} = local density relative to the average density

\bar{g} = gravitational vector, and

\bar{D} = structural drag vector.

The coefficients of viscosity, μ and λ , which appear in the viscous stress tensor, e.g.,

$$\sigma_{rr} = 2\mu \frac{\partial u}{\partial r} - \lambda \nabla \cdot \bar{u} \quad (3)$$

where λ is $2/3\mu$, and μ is interpreted as the "eddy viscosity," are defined by the simple algebraic turbulence model $\nu = \mu/\rho = 1/40 s \sqrt{2q}$. In this model, s is equal to a length scale (1.50 m for these calculations) and $\sqrt{2q}$ is the turbulent energy intensity (0.15| \bar{u} | for these calculations), so $\mu = 0.56 \rho |\bar{u}|$. The structural drag vector is given by $\bar{D} = C_D \rho (\text{Area/Volume}) \bar{u} |\bar{u}|$, where Area/Volume = (structure area)/(structure volume), and $C_D = 1$. The mixture internal energy density equation is

$$\frac{\partial(\rho I)}{\partial t} + \nabla \cdot (\rho I \bar{u}) = - \rho \nabla \cdot \bar{u} + \nabla \cdot (\kappa \nabla T) + Q \quad (4)$$

where

I = mixture specific internal energy

κ = "eddy conductivity,"

T = mixture temperature, and

Q = energy source and/or sink per unit volume and time.

The Species Transport Equations

The dynamics of the individual species are determined by

$$\frac{\partial \rho_{H_2}}{\partial t} + \nabla \cdot (\rho_{H_2} \bar{u}) - \nabla \cdot \left[\rho \gamma \nabla \left(\frac{\rho_{H_2}}{\rho} \right) \right] = S_{H_2} + S_{O_2} \quad (5)$$

$$\frac{\partial \rho_{N_2}}{\partial t} + \nabla \cdot (\rho_{N_2} \bar{u}) - \nabla \cdot \left[\rho \gamma \nabla \left(\frac{\rho_{N_2}}{\rho} \right) \right] = 0 \quad (6)$$

$$\frac{\partial \rho_{H_2O}}{\partial t} + \nabla \cdot (\rho_{H_2O} \bar{u}) - \nabla \cdot \left[\rho \gamma \nabla \left(\frac{\rho_{H_2O}}{\rho} \right) \right] = - S_{H_2} \quad (7)$$

and

$$\frac{\partial \rho_{O_2}}{\partial t} + \nabla \cdot (\rho_{O_2} \bar{u}) - \nabla \cdot \left[\rho \gamma \nabla \left(\frac{\rho_{O_2}}{\rho} \right) \right] = - S_{O_2} \quad (8)$$

where the "eddy diffusivity", γ , is determined by setting the Schmidt Number to unity, $\gamma = \mu/\rho$, and S_{H_2} and S_{O_2} are determined by the chemical kinetics presented below. Summing the above species transport equations results in the mixture mass conservation equation.

Chemical Kinetics

We are employing global chemical kinetics in which the only reaction modelled is $2H_2 + O_2 \xrightarrow{\dot{\omega}} 2H_2O + \dot{Q}$, which is similar to the chemical kinetics models in other Los Alamos combustion codes [6-8]. Hydrogen combustion models by means of many more elementary reaction steps and intermediate chemical species. The chemical reaction time scale is, however, very short compared with fluid dynamic motions and meaningful calculations can be accomplished using this simplified global chemical kinetics scheme [9]. Here, \dot{Q} is the chemical energy of combustion per unit volume and time, i.e., $\dot{Q}_c \left[\frac{J}{m^3} \right] = 4.178 \times 10^5 \left[\frac{J}{mole} \right] \dot{\omega} \left[\frac{mole}{m^3 \cdot s} \right]$. The reaction rate, $\dot{\omega}$, is modeled by

Arrhenius kinetics as

$$\dot{S} = C_f \left[\frac{2}{M} \right]_{H_2} \left[\frac{2}{M} \right]_{O_2} \exp(-10^4/T) \quad (9)$$

where M is the molecular weight and $C_f = 3.3 \times 10^5 \left[\frac{m^3}{mole \cdot s} \right]$. Now, the source terms S_H and S_O are found by $S_{H_2} = 2H_2 \dot{S}$, and $S_{O_2} = H_{O_2} \dot{S}$.

III. EXAMPLE: HYDROGEN MIXING IN THE EPRI/HEDL STANDARD PROBLEMS

The HYS code was used to analyze the EPRI/HEDL standard problems "A" and "B" [10]. These standard problems were proposed as a bases for comparing blind predictions of detailed hydrogen distribution in reactor-like containment compartments. In both experiments a high velocity steam-hydrogen or steam-helium jet is released into the compartment. The reader is referred to Ref. 11 for a detailed discussion of the experimental facility.

Figure 1 presents the discretization of the containment compartment. We have modeled the blower which provides recirculation from the upper to lower compartments as four time-dependent prescribed inflow boundary cells. Flow is allowed to exit the computational mesh by the eight continuative outflow boundary cells shown on the outer circumference. Both tests started with the compartment at 65°C and 10^5 Pa, with test A containing nitrogen and test B containing air.

Experiment A had a horizontal steam-hydrogen jet that was centered in the annulus at 75° at a height 1.52 m from the floor. The average jet velocity was assumed to be 150 m/s, and it was directed inward at 90° to a radial ray. Experiment B had a vertical steam-helium jet that was located at 180°, 1.2 m from the floor, and 2.31 m from the compartment axis. The average jet velocity was assumed to be 80 m/s.

In Figs. 2 and 3, we present the test data and the blind (i.e., pretest) concentration predictions for tests A and B, respectively. The curve designated "E" represents the experimental data while the curve designated "C" represents the calculation. For test A, the horizontal jet, there is total mixing throughout the compartment as evidenced by the similarity of the concentration curves and maximum concentrations at various locations in the compartment. All concentrations in this paper are reported in volume percent on a dry basis; i.e., the steam was condensed and the gas sample passed through a drying bed in the tests. Concentrations for test B, the vertical jet, are presented for the same locations as test A. Here we see a definite concentration gradient of roughly 2 to 3 concentration percent during the gas injection phase with maximum values at the compartment top and minimum values at the bottom. This gradient quickly decays to about 1% after the jet is shut off. Our blind calculations of the concentrations are seen to predict the experimental data very well.

IV. EXAMPLE: NUMERICAL CALCULATION OF HYDROGEN-AIR COMBUSTION [12]

The following calculations of hydrogen-air mixtures burning in a closed cylinder were performed by CHIMERE-SPRAY. The vessel is roughly 5 m high and 2 m in diameter with its axis orientated in the vertical direction. Uniform hydrogen-air mixtures were introduced into the vessel and ignition occurred on the axis about 1 m from the base. Two types of behavior were observed in the experiment and reproduced in the computer calculations. When the initial quantity of hydrogen was small, i.e., 7.5% hydrogen by volume as shown in Fig. 4, then the pressure history had two peaks. When higher initial hydrogen quantities were used, i.e., 10.7% hydrogen by volume as shown in Fig. 5, then a single sharp pressure spike was observed.

We can describe the events of these two cases by interpreting the isotherm plots associated with various times in both calculations. The temperature values of each isotherm are equally spaced between the hottest and lowest values, which are given below each plot. The time associated with each plot is given above it.

We first detail the sequences of events depicted in the isotherm plots. Ignition in both calculations occurs at 0.0 seconds. With 7.5% hydrogen, at 1.99 seconds the flame completely surrounds the hot burner and gases and separates them from the cool, unburned gases. Buoyancy has caused the burn-product gases to rise to the point of ignition more than half the height of the cylinder, and the region they occupy has reformed into a mushroomlike shape. The burn products rise until the flame simultaneously reaches the top and side walls of the cylinder at 2.84 seconds. Subsequently the flame becomes more planar and propagates downward into the still remaining unburned gases, which now lie at the bottom of the cylinder, as in the plot at 4.91 seconds. The isotherms in this plot also show lower temperatures near the walls caused by conduction of heat from the hot burn-product gases to the cooler walls. Burning is complete in this calculation shortly after 8.0 seconds.

The sequence of events for 10.7% hydrogen differs considerably from that described above. Because of the increased amount of hydrogen in the initial mixture, the flame propagates more quickly into the unburned gases. Thus at 1.01 seconds the flame already reaches the outer walls, it separates into two flames that propagate upward and downward in the cylinder. These reach the top and bottom walls of the cylinder at nearly the same time, as shown in the plot at 1.91.

Two competing effects cause changes in the pressure in the cylinder in both experiments: heat release from chemical reactions in the flame and conductive heat loss from the hot combustion gases to the walls of the cylinder. The first effect causes the pressure to rise; the second causes the pressure to drop. The rate of heat release depends on the speed of propagation of the flames and the surface area associated with the flames. The

surface area is roughly equal to the area associated with an isotherm contour that lies in the flame zone. Higher flame speeds and larger associated surface areas cause the pressure to rise faster.

We can now explain the cause of what we see in the measured pressure histories. With 7.5% hydrogen, the pressure rises slowly at first because of the low speed and the small surface area associated with the flame. As the flame approaches the outer walls, its surface area increases, and the rate of the pressure rise increases as a consequence. The rate of pressure rise reaches its maximum when the flame area is largest, just before it reaches the top and side walls at 2.88 seconds. After burn-out to the walls, the rate of pressure rise is less because the surface area associated with the flame is reduced and because the hot burn-product gases are now in contact with and losing heat to the walls of the cylinder. The small drop in pressure between 3.0 and 4.0 seconds in the experiment may be due to high velocities near the walls that enhance heat transfer rates, an effect that is not accurately modeled in the calculation. After 3.0 seconds the flame propagates downward very slowly because wall heat loss cools the gases behind the flame. The flame speed, a very sensitive function of temperature, slows when the temperature drops. When burning is complete at 8.0 seconds, wall heat loss causes the pressure to drop.

With 10.7% hydrogen, the pressure also rises slowly at first and then accelerates as the flame surface area increases. However, the pressure continues to rise steeply after the flame reaches the outer walls. Thus the overall rate of chemical heat release remains large even though, after burn-out to the walls, the flame surface area is smaller and wall heat losses are occurring. A more detailed analysis of the calculation then we give here shows that several physical effects are responsible for this continued large heat-release rate. One of these is clear from the isotherm plots: after burn-out to the walls, the surface area associated with the flames is larger with 10.7% hydrogen than it is with 7.5% hydrogen.

V. HYDROGEN DIFFUSION FLAMES IN A REACTOR CONTAINMENT

It has recently become of interest to analyze hydrogen diffusion flames in reactor containments [4]. In this accident sequence, a transient event from 100% power is followed by loss of all coolant-injection capability. The reactor vessel remains pressurized as the coolant water in the reactor vessel begins to boil away. When the core becomes uncovered and heats up, after roughly 40 minutes into the accident, zirconium and steel oxidation leads to the generation of hydrogen which is then released through safety relief valves into the suppression pool. Under certain conditions, this release of hydrogen (e.g., with an ignition source) leads to the formation of diffusion flames above the release areas in the suppression pool. These flames may persist in localized regions above the suppression pool for tens of minutes and therefore could lead to overheating of nearby penetrations in the dry-well or wet-well walls. It is of most interest to calculate the temperature and pressure of the containment atmosphere in the wet-well region and the heat flux loads on the dry-well and wet-well walls up to 10 m above the suppression pool surface.

The reactor containment design in question is shown schematically in Fig. 6. We are only concerned with the containment volume above the water level so we approximate the containment with the configuration presented in Fig. 7, which has the same atmospheric containment volume as that of Fig. 6. The outer vertical containment wall (wet-well wall) is concrete 0.75 m (2.5 feet) thick and the inner vertical wall (dry-well wall) is concrete 1.5 m (5 feet) thick. The annular region between these two walls is called the wet-well. Hydrogen spargers or sources are actually at the bottom of the suppression pool within 3 m of the inner wall. The nine sources can be thought of as circular, 3 m diameter, centered azimuthally at 16, 48, 88, 136, 152, 184, 256, 288, and 328 degrees. Fig. 8 gives the idea of the sources relative to the wet-well and the containment walls.

The geometry as shown in the two perspective views of Figs. 9 and 10 indicates the true three-dimensionality of the containment. The hydrogen sources are shown at the bottom as rectangular regions. The cylindrical computational mesh approximating this geometry is presented in Fig. 11 which shows each of the computing zones. A pipe-shaped region of the computing mesh indicating the dimensions is presented in Fig. 12. Hydrogen enters the computing mesh at the bottom ($J=2$) of specific cells in the annular ring ($I=8$) with a temperature equalling 71°C and pressure equalling 10^5 Pa. The azimuthal positions of the hydrogen sources within the ring $I=8$ are specified at $K = 4, 6, 8, 13, 15, 16, 20, 22$, and 24 which corresponds to computational zones centered at $322.5, 292.5, 262.5, 187.5, 157.5, 142.5, 82.5, 52.5$, and 22.5 degrees, respectively. A mass flow rate of 45.5 kg/min is distributed equally among the nine sources. The initial condition in the containment is dry air at 21°C and 10^5 Pa.

There are tremendous heat sinks in the containment, e.g., 2.2×10^6 kg steel with heat transfer surface area equalling 2.7×10^4 m², from which an average surface area per unit volume can be found. The structural heat transfer and drag formulations both use this average value to compute heat and momentum exchange, respectively, within a computational zone.

Figure 13 displays velocity vectors in an unwrapped (constant radius vs. height) configuration. The pictures in at the radial center of the hydrogen source cells ($I=8$), which can be seen at the bottom of each plot by the openings. For example, there is a double source between 135 and 165 degrees and seven single sources distributed along the azimuthal dimension. With nine distributed sources, and distributed as they are, Fig. 13 shows the development of very strong buoyancy driven flows in the partial hot chimney at 45 degrees and the full hot chimneys at 135 and 315 degrees. A cold chimney (downflow) develops at 225 degrees completing the convective loops. The flow in the partial hot chimney (45 degrees) is blocked by a concrete floor about half way to the top and is diverted toward the outer wall and upward around the enclosed volumes shown in this figure. The horizontal lines designate concrete floors where no mass, momentum or energy is allowed to flux across these lines. Thus we see the hot products of combustion beneath the floors at say 270 degrees convecting horizontally and contributing to the full hot chimney at 315 degrees. Maximum gas temperatures are generally found in regions of multiple sources and beneath concrete floors as depicted in Fig. 14. Note that the contour plotting routine does not resolve the concrete floors which are thin compared to the cell height. The resolution under the floors is insufficient to actually show any contours; however, the idea of high/low concentrations and gradients is clearly demonstrated.

Early in the calculation, 120 s, most of the hydrogen combusts in the inlet computational zone as shown by the hydrogen density contour plot of Fig. 15. This is confirmed by the chemical energy contour plot (Fig. 16) which shows the energy of combustion in the nine source inlet regions and the oxygen density contour plot (Fig. 17) showing low values near combustion regions and high values in the cold chimney (225 degrees). At later times (1410 s), Figs. 18-22 show the same overall flow pattern, but only hydrogen sources near the cold chimney are continuing to combust in the inlet regions. The others which have become oxygen starved are combusting higher up in the wet-well. This is shown best in Fig. 19 where maximum gas temperatures are found far above the pool surface.

Summary results are presented in the next figures. Figure 23 shows the maximum and minimum wet-well temperatures and containment atmosphere pressure. Note that the maximum temperature would always be the adiabatic flame temperature for the composition of gases at that particular time. We correctly calculate the adiabatic flame temperature; however, because of the coarseness of the computational mesh, the temperature of any zone in which combustion is taking place will always be lower than the actual adiabatic flame temperature. Mass histories for H_2O , H_2 , and O_2 are also included in Fig. 23. Note that at roughly 1600 s, oxygen is totally depleted in the containment. Spatial distributions for heat fluxes to the inner and outer wet-well walls at 3.3 m (11 feet) and 10 m (30 feet) above the pool surface are presented in Fig. 24 for various times (30, 120, 600, and 1800 seconds). The hydrogen sparger or source azimuthal positions are indicated on each figure, where maximum heat flux values correspond one for one to the sparger locations. For azimuthal locations 142.5 and 292.5 degrees where large values of the heat flux occur, we have given heat flux histories in Fig. 25 at the 3.3 m and 10 m levels above the suppression pool surface for both inner and outer walls. The heat fluxes on the inner wall peak early and then decrease as heat is convected to other regions of the containment. Most of the heat transferred to the outer wall is radiated to these surfaces from the burning hydrogen.

Without a flame model or resolving flame details with a finely zoned computational mesh, it is impossible for us to supply details about the flame such as flame height, flame width and flame angle. We can say, however, that most of the combustion takes place in the inlet cell (flame height 6 m), as long as there is sufficient oxygen for combustion. Once flames become oxygen starved, then it is possible for flames to lift off the water surface and burn higher in the wet-well, perhaps even reattaching to the water surface as more oxygen is supplied by convection.

VI. CONCLUSION

Detailed analyses of hydrogen transport, mixing, and combustion in containments is now possible. In conserving mass, momentum and energy throughout the containment, these time-dependent, two- and three-dimensional calculations are in very good agreement with available data; in fact, these calculations should be considered benchmark analyses.

VII. ACKNOWLEDGMENTS

This work was performed under the auspices of the United States Nuclear Regulatory Commission.

VIII. REFERENCES

1. L. D. Cloutman, J. K. Dukowicz, J. D. Ramshaw, and A. A. Amsden, "CONCHAS-SPRAY: A Computer Code for Reactive Flows with Fuel Sprays," Los Alamos National Laboratory report LA-9294-MS (May 1982).
2. J. R. Travis, "HMS: A Model for Hydrogen Migration Studies in LWR Containments," Second Intern. Workshop on the Impact of Hydrogen on Water Reactor Safety, October 3-7, 1982, Albuquerque, NM.
3. J. R. Travis, "HMS: A Computer Program for Transient, Three-Dimensional Mixing Gases," Los Alamos National Laboratory report in preparation.
4. J. R. Travis, "Hydrogen Diffusion Flames in a Mark-III Containment," ANS/ASME Conference on Design, Construction, and Operation of Nuclear Power Plants, Portland, Oregon, August 5-8, 1983.
5. J. R. Travis, "HMS-Burn: A Transient, Three-Dimensional Computer Program for Transport, Mixing, and Combustion of Hydrogen in Containments," Los Alamos National Laboratory report in preparation.
6. W. C. Rivard, O. A. Farmer, and T. D. Butler, "RICE: A Computer Program for Multicomponent Chemically Reactive Flows at All Speeds," Los Alamos Scientific Laboratory report LA-5812 (March 1975).
7. J. D. Ramshaw and J. K. Dukowicz, "APACHE: A Generalized-Mesh Eulerian Computer Code for Multicomponent Chemically Reactive Fluid Flow," Los Alamos Scientific Laboratory report LA-7427 (January 1979).
8. T. D. Butler, L. D. Cloutman, J. K. Dukowicz, and J. D. Ramshaw, "CONCHAS: An Arbitrary Lagrangian-Eulerian Computer Code for Multicomponent Chemically Reactive Fluid Flow at All Speeds," Los Alamos Scientific Laboratory report LA-8129-MS (November 1979).
9. T. D. Butler, L. D. Cloutman, J. K. Dukowicz, and J. D. Ramshaw, "Multi-dimensional Numerical Simulation of Reactive Flow in Internal Combustion Engines," *Prog. Energy Combust. Sci.* 7, 293 (1981).

10. J. R. Travis, "Hydrogen Migration Modeling for the EPRI/HEDL Standard Problems," Tenth Water Reactor Safety Research Information Meeting, Gaithersburg, Maryland, October 12-15, 1982.
11. G. R. Bloom, L. D. Muhlestein, and A. K. Postma, "Hydrogen Distribution in a Compartment with a High Velocity Hydrogen-Steam Source," Second Intern. Workshop on the Impact of Hydrogen on Water Reactor Safety, October 3-7, 1982, Albuquerque, NM.
12. P. J. O'Rourke, "Numerical Calculations of Hydrogen-Air Combustion," Los Alamos National Laboratory Mini-Review, LALP-83-25, August 1983.

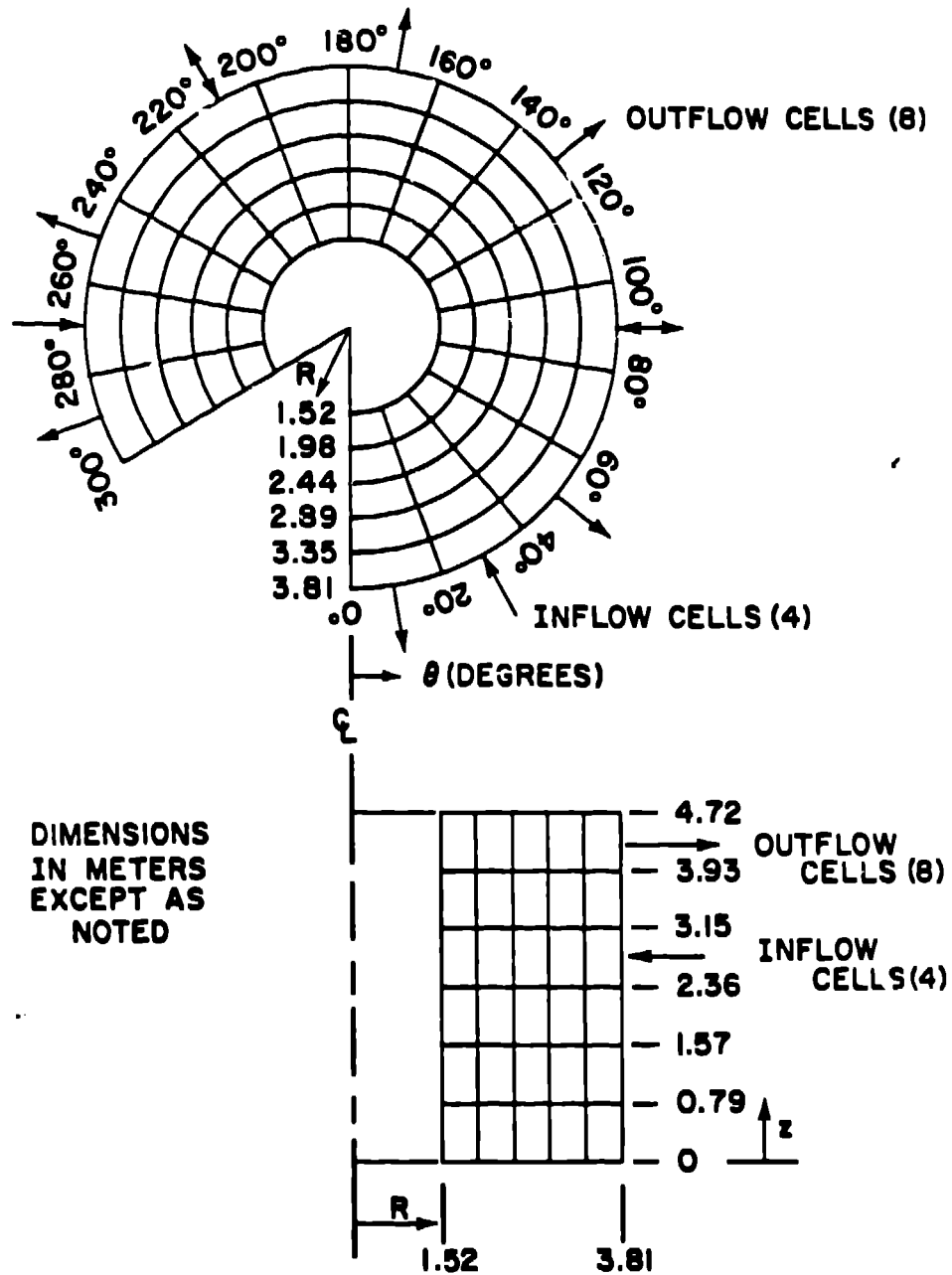


Fig. 1 RMS computing mesh for EPRI/HEDL Standard Problems A and B.

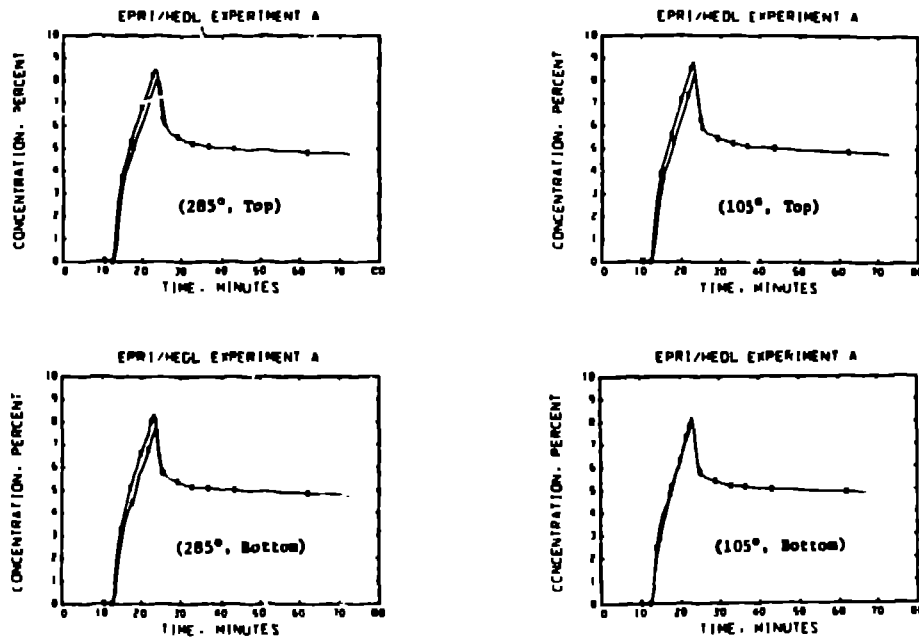


Fig. 2 Hydrogen concentrations for Test A on a dry basis for the indicated locations. The Top and Bottom designations are 0.23 m below the ceiling and 0.3 m above the lower deck, respectively. The curves labeled "x" depict experimental data and those labeled "o" represent the blind calculated results.

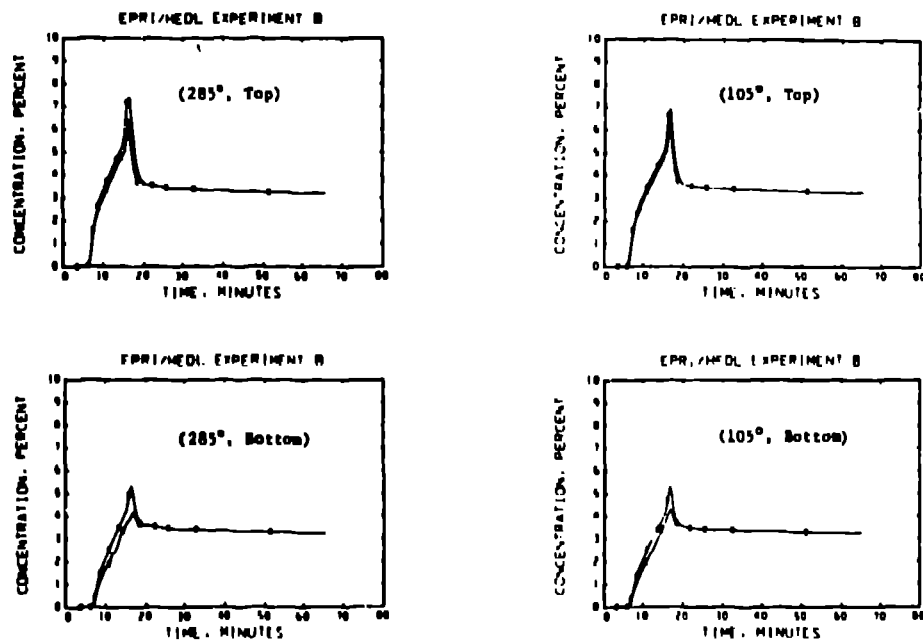


Fig. 3 Helium concentrations for Test B on a dry basis for the indicated locations. The Top and Bottom designations are 0.23 m below the ceiling and 0.3 m above the lower deck, respectively. The curves labeled "x" depict experimental data and those labeled "o" represent the blind calculated results.

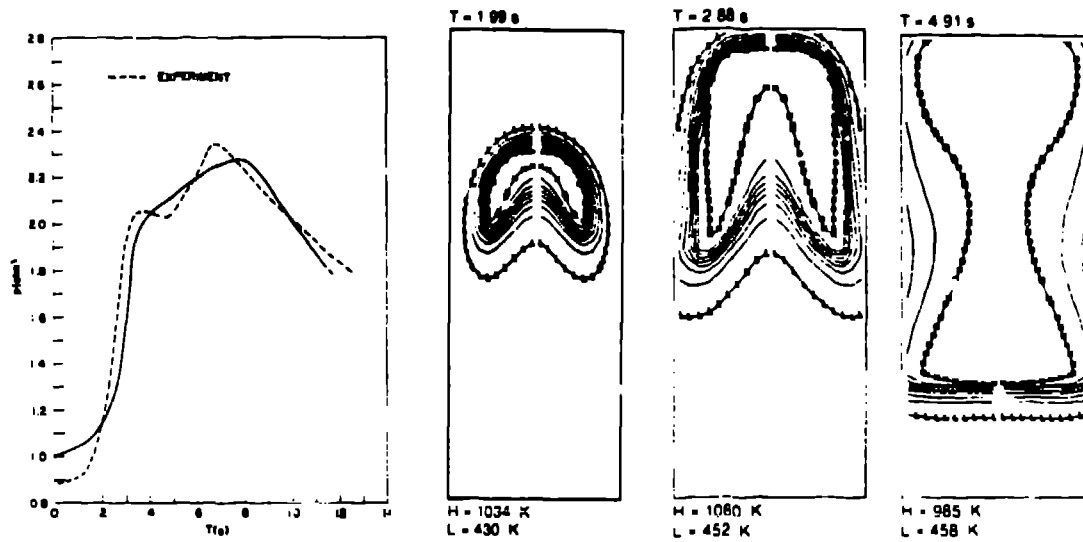


Fig. 4 Premixed 7.5% Hydrogen by Volume and Air. Pressure History and Isotherms at Various Times.

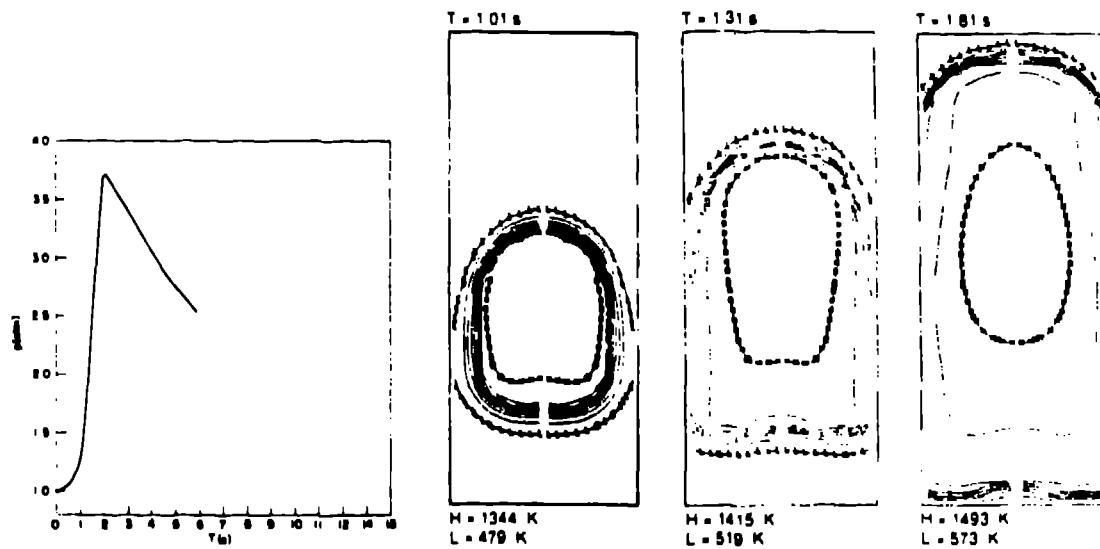


Fig. 5 Premixed 10.7% Hydrogen by Volume and Air. Pressure History and Isotherms at Various Times.

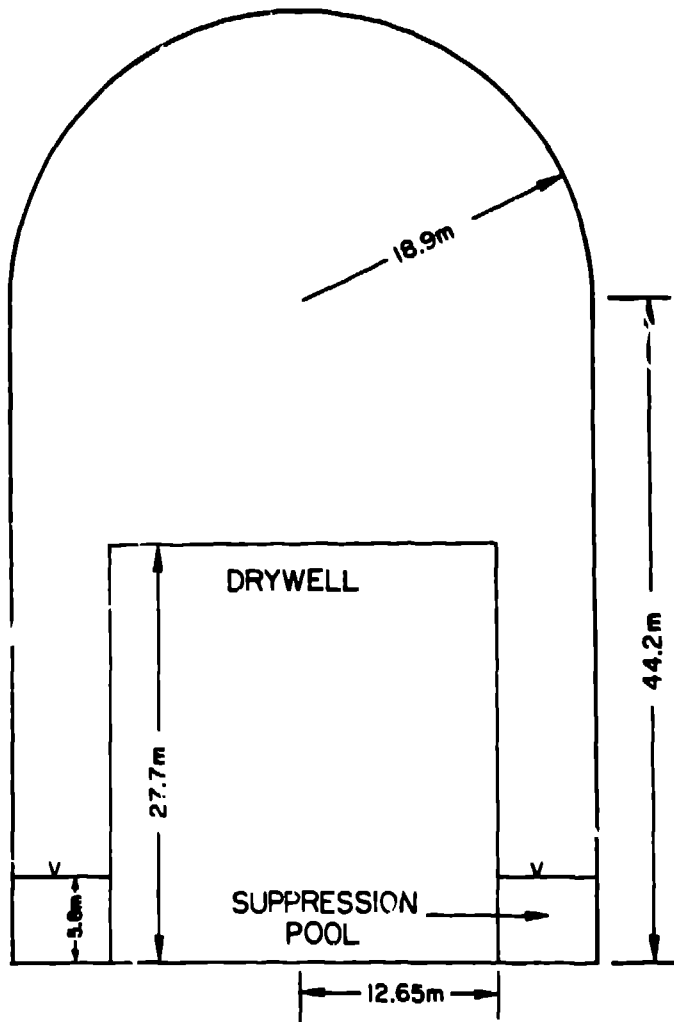


FIG. 6 Schematic View of the MARK-III Containment Design showing the Suppression Pool and the Wet-well (Annular Region above the Pool).

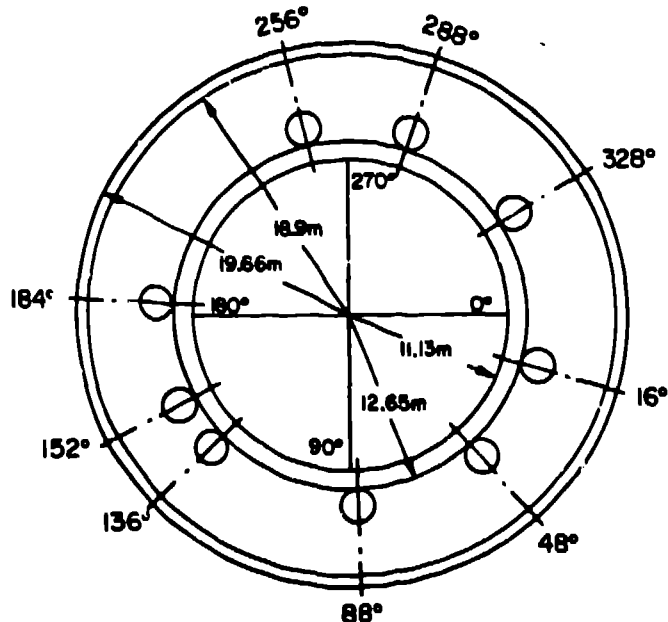


FIG. 8 Schematic View of the MARK-III Containment Design showing the Nine Hydrogen Spargers (sources) Relative to the Wet-well.

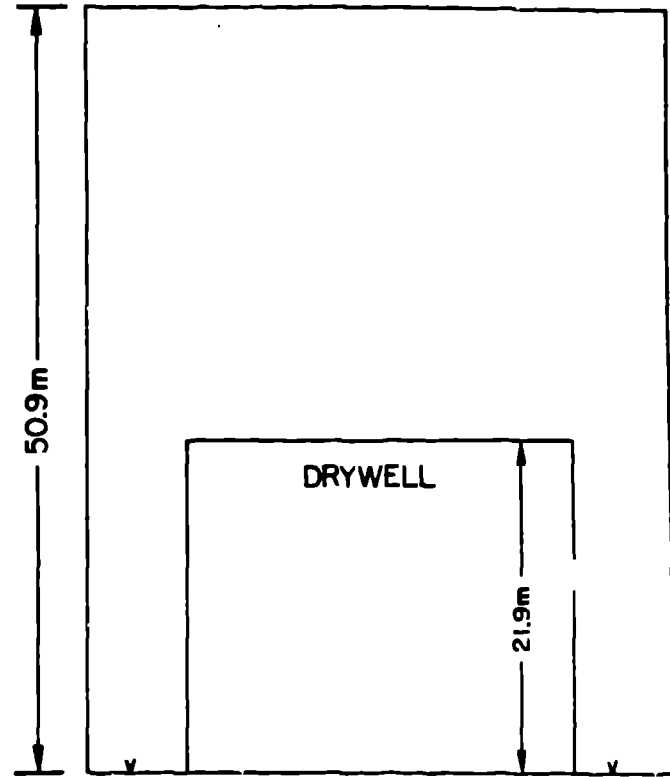


FIG. 7 Schematic View of the MARK-III Containment Design showing the geometry used in the Calculation. Note that the Containment Volumes are Equal in Figs. 2 and 3.

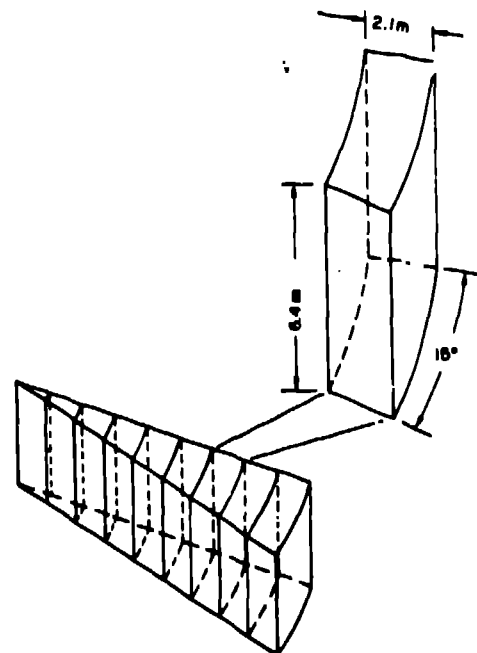


FIG.12 Perspective View of a Pie Shaped Zone within the Computing Mesh.

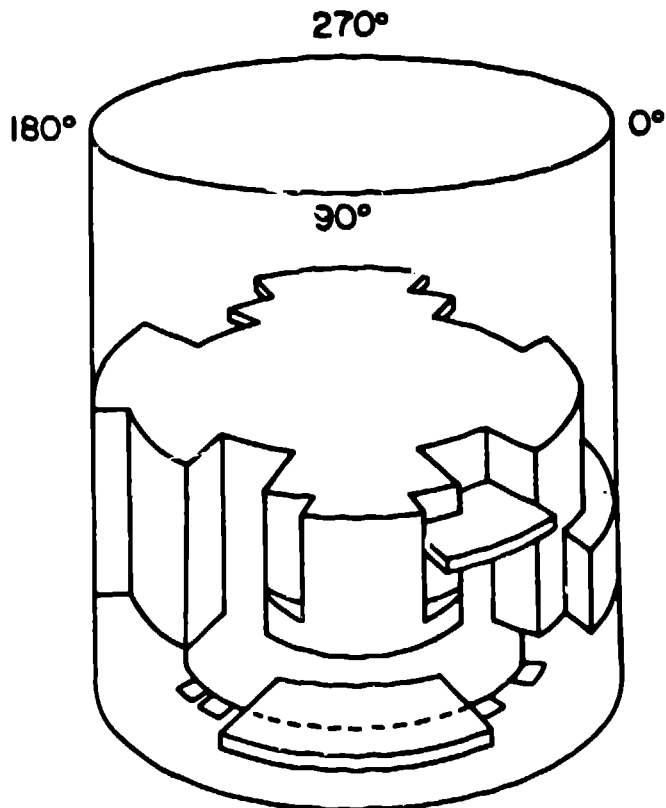


FIG. 9 Perspective Front View of Containment showing Excluded Volumes, Concrete Floors, and Locations of Hydrogen Sources.

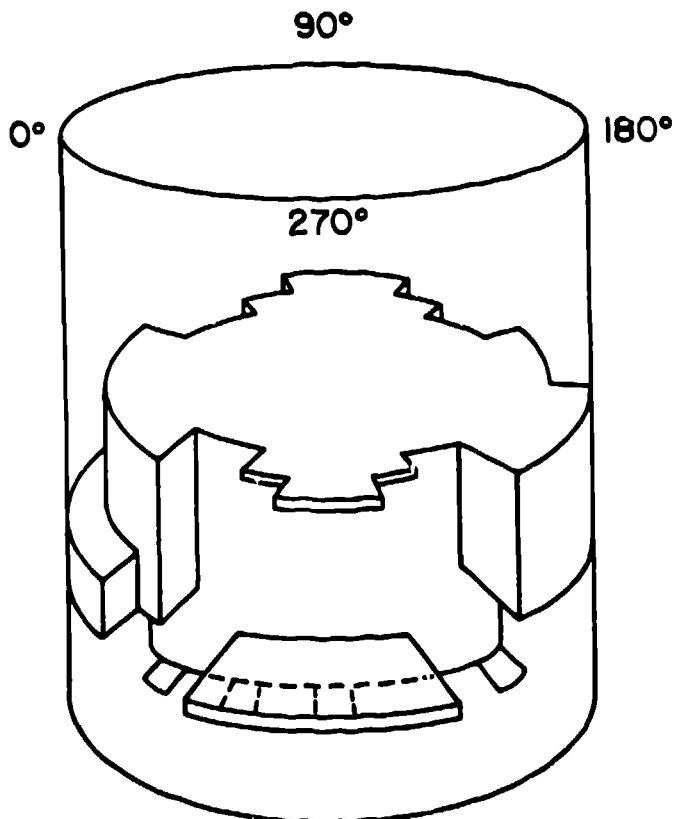


FIG. 10 Perspective Back View of Containment showing Excluded Volumes, Concrete Floors and Locations of Hydrogen Sources.

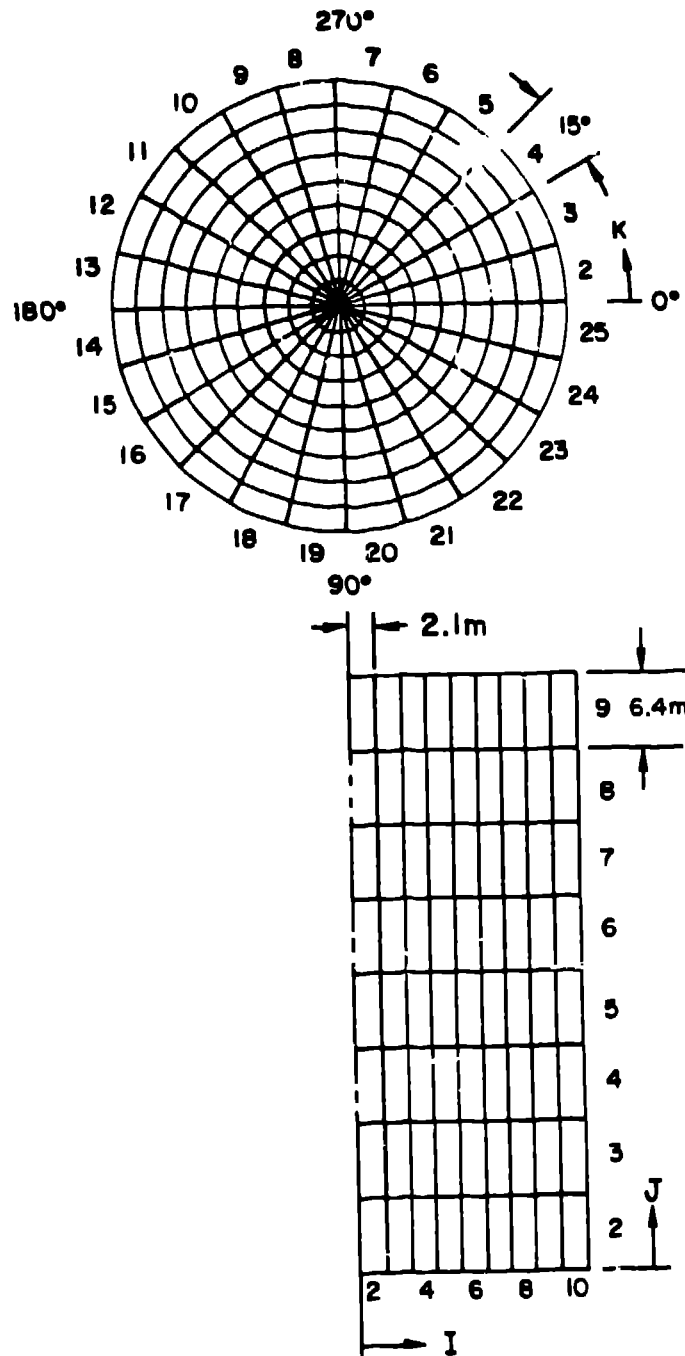


FIG. 11 Computing Mesh for Containment Geometry.

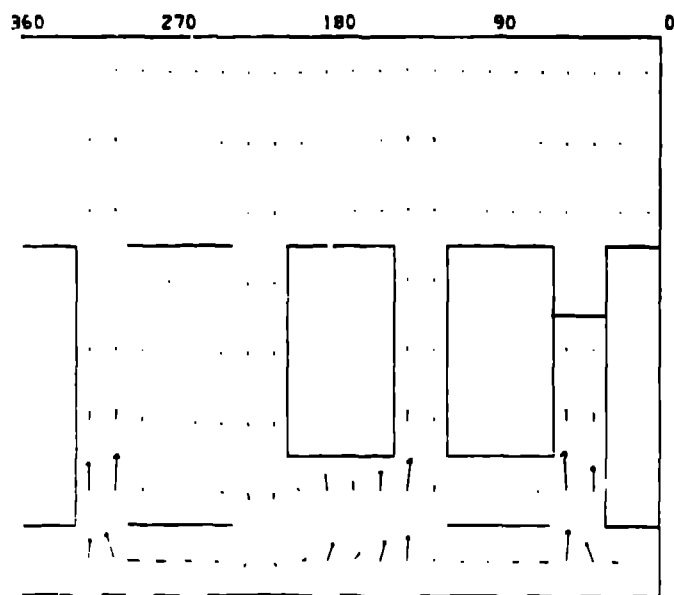


FIG. 13 Unwrapped (axial dimension, z vs. constant radius, $I=8$) Velocity Vectors at 120 s.
 $V_{\max} = 7.3 \text{ m/s}$ and $W_{\max} = 2.9 \text{ m/s}$.

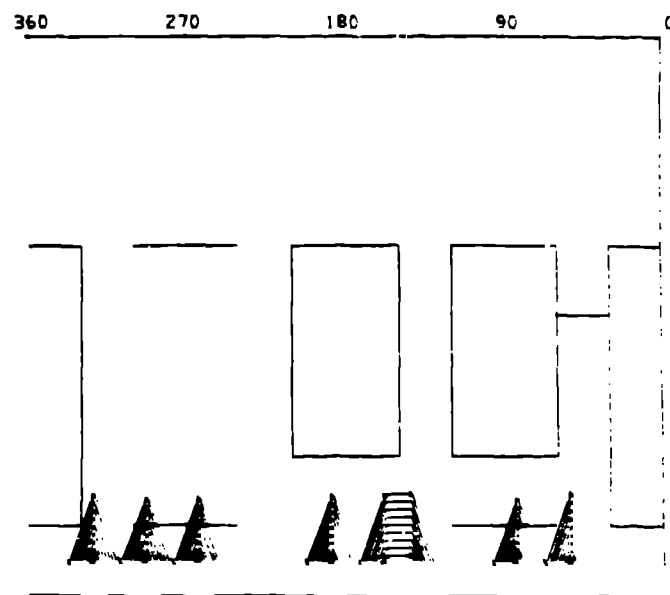


FIG. 15 Unwrapped (axial dimension, z vs. constant radius, $I=8$) Hydrogen Density Contours at 120 s.
 $H = 1.5 \times 10^{-4} \text{ kg/m}^3$ and $L = 0.0 \text{ kg/m}^3$.

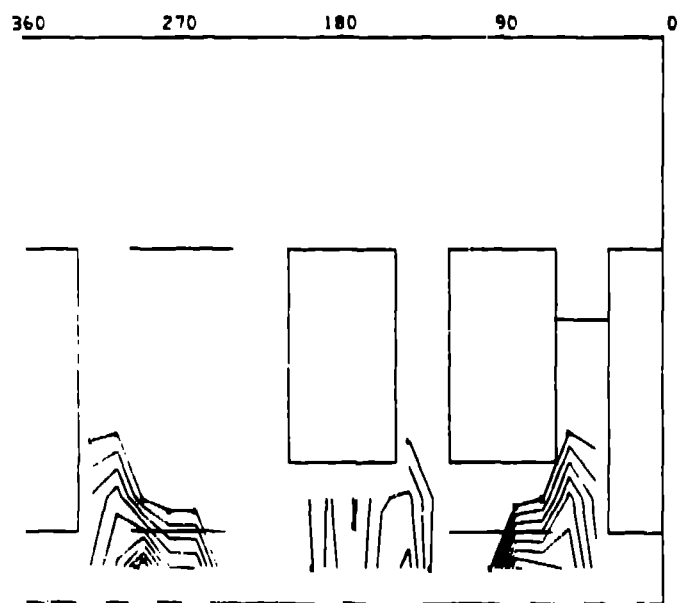


FIG. 14 Unwrapped (axial dimension, z vs. constant radius, $I=8$) Gas Temperature Contours at 120 s.
 $H = 1256$ and $L = 294$.

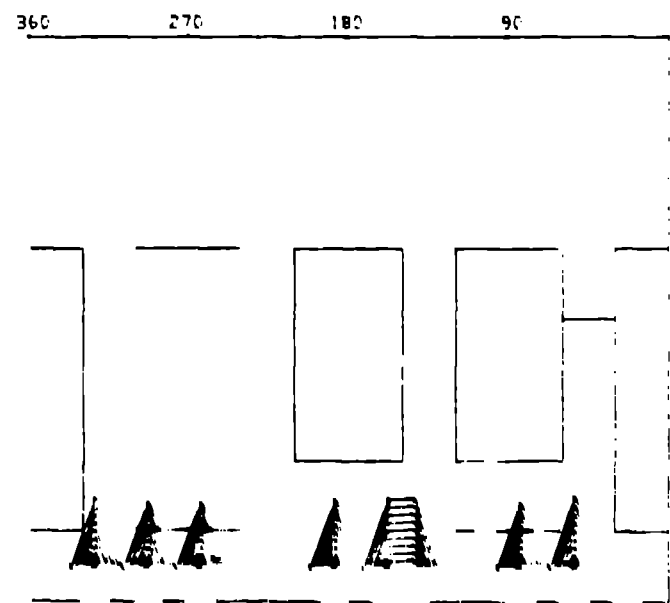


FIG. 16 Unwrapped (axial dimension, z vs. constant radius, $I=8$) Chemical Energy of Combustion Contours at 120 s. $H = 1.8 \times 10^5 \text{ W/m}^3$ and $L = 0.0 \text{ W/m}^3$.

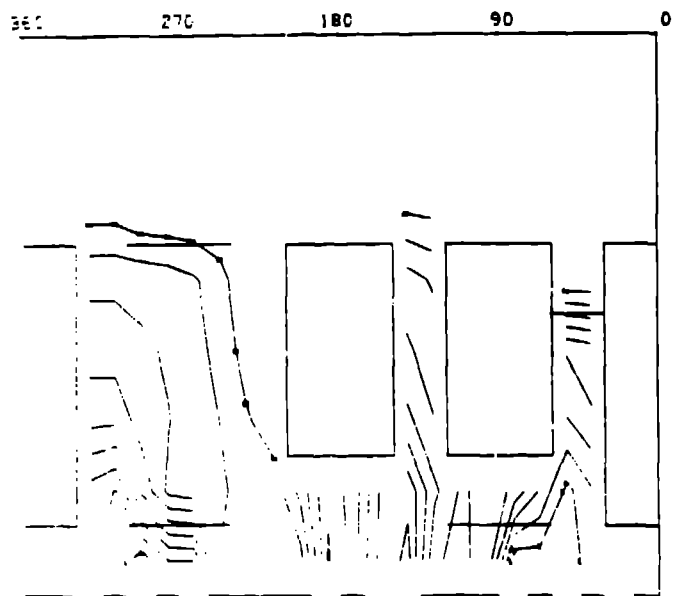


FIG. 17 Unwrapped (axial dimension, z vs. constant radius, 1=8) Oxygen Density Contours at 120 s.
 $H = 2.9 \times 10^{-1} \text{ kg/m}^3$ and $L = 2.0 \times 10^{-2} \text{ kg/m}^3$.

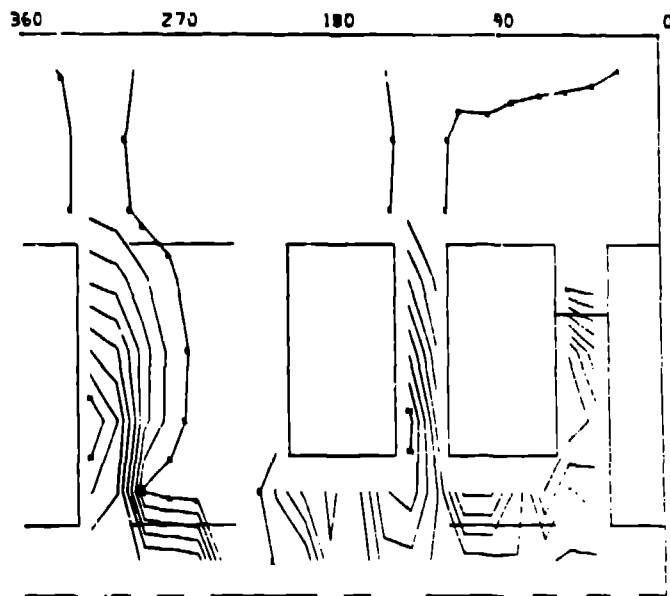


FIG. 19 Unwrapped (axial dimension, z vs. constant radius, 1=8) Gas Temperature Contours at 1410 s.
 $H = 784$ and $L = 297$.

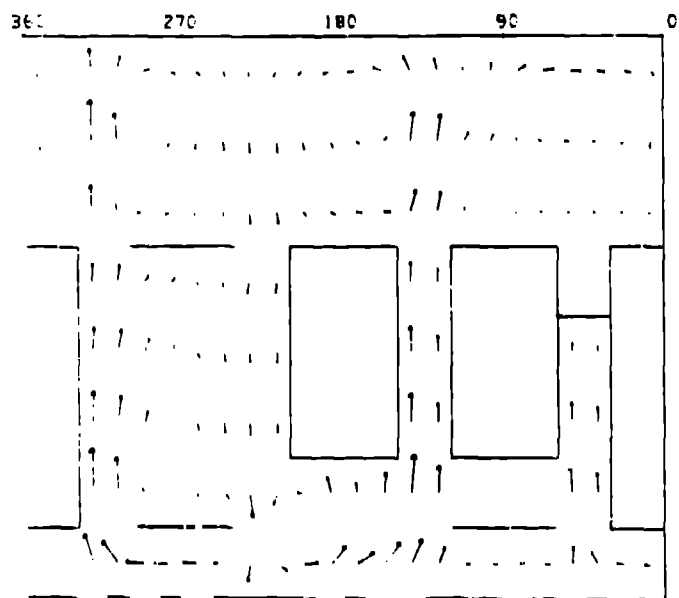


FIG. 18 Unwrapped (axial dimension, z vs. constant radius, 1=8) Velocity Vectors at 1410 s.
 $V_{\max} = 3.8 \text{ m/s}$ and $W_{\max} = 2.2 \text{ m/s}$.

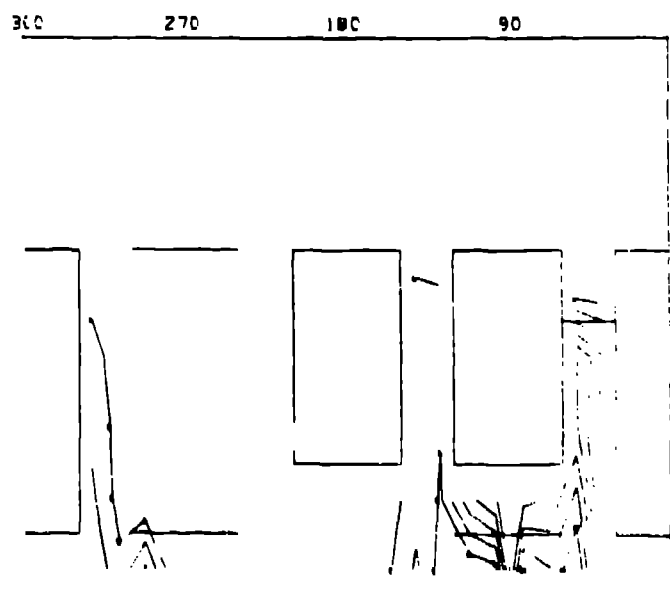


FIG. 20 Unwrapped (axial dimension, z vs. constant radius, 1=8) Hydrogen Density Contours at 1410 s. $H = 8.5 \times 10^{-3} \text{ kg/m}^3$ and $L = 0.0 \text{ kg/m}^3$.

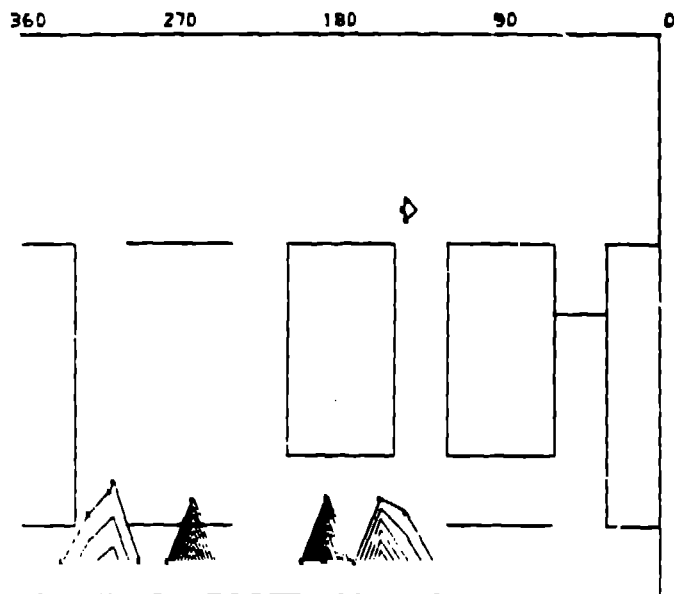


FIG. 21 Unwrapped (axial dimension, z vs. constant radius, $l=8$) Chemical Energy of Combustion Contours at 1410 s. $H = 1.8 \times 10^5 \text{ W/m}^3$ and $L = 2 \times 10^{-11} \text{ W/m}^3$.

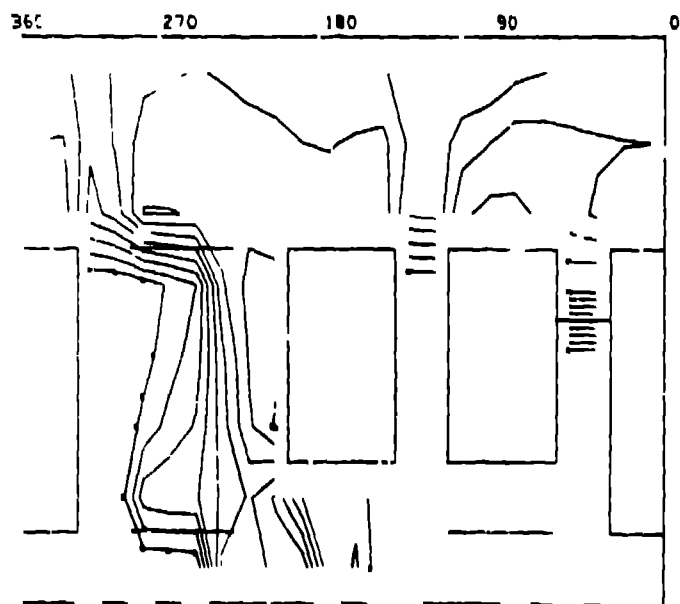


FIG. 22 Unwrapped (axial dimension, z vs. constant radius, $l=8$) Oxygen Density Contours at 1410 s. $H = 5.9 \times 10^{-2} \text{ kg/m}^3$ and $L = 0.0 \text{ kg/m}^3$.

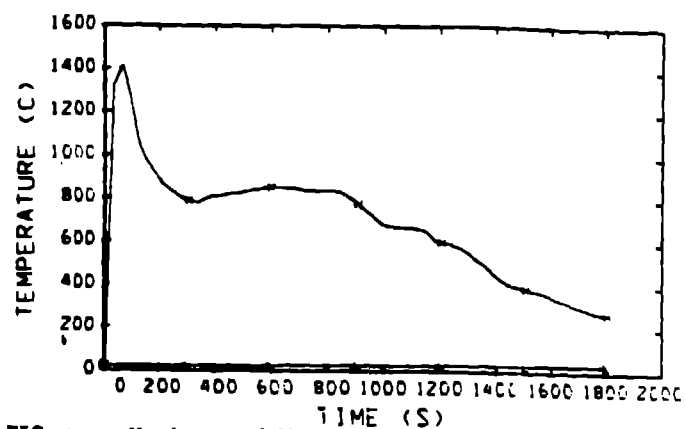


FIG. 23a Maximum and Minimum Atmospheric Wet-well Temperatures.

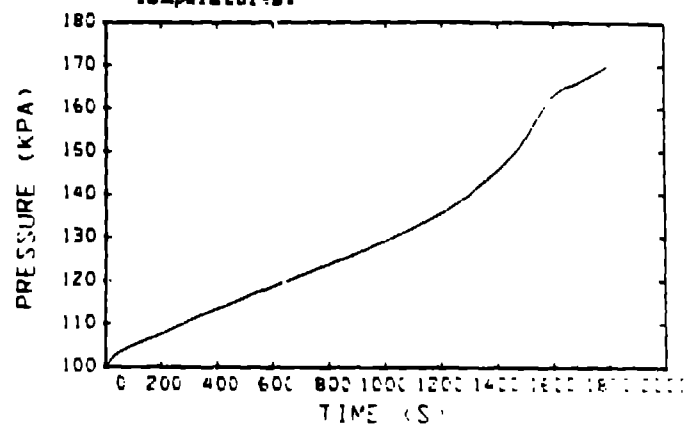


FIG. 23b Maximum Containment Pressure.

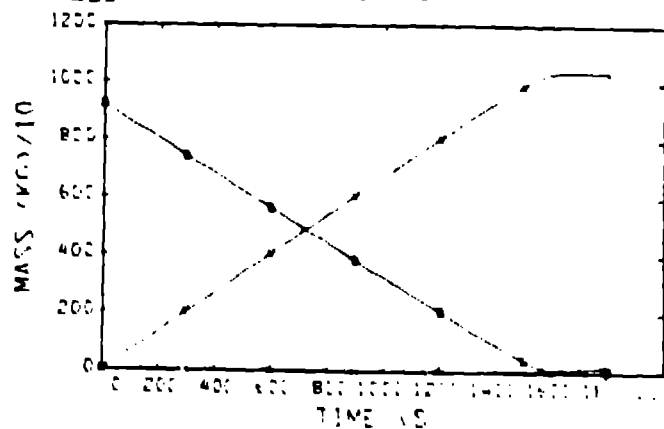


FIG. 23c Mass of O_2 , H_2O , and H_2 in Containment.

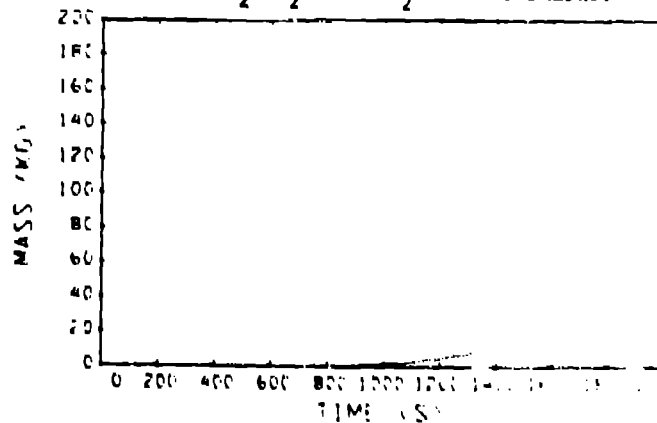


FIG. 23d Mass of H_2 in Containment.

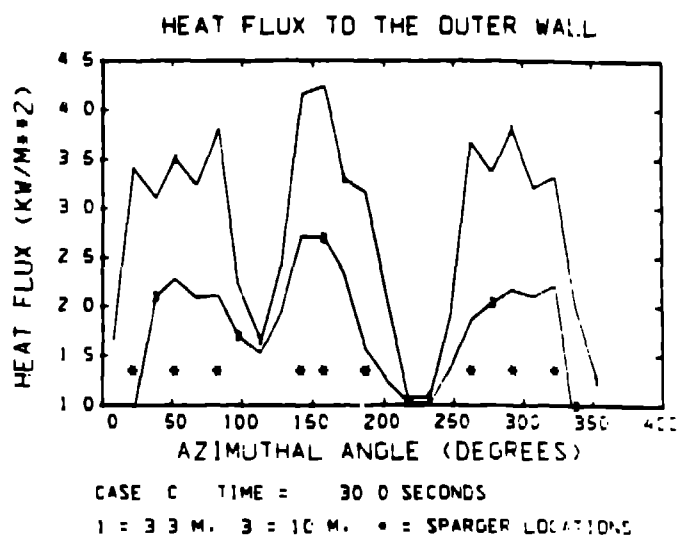
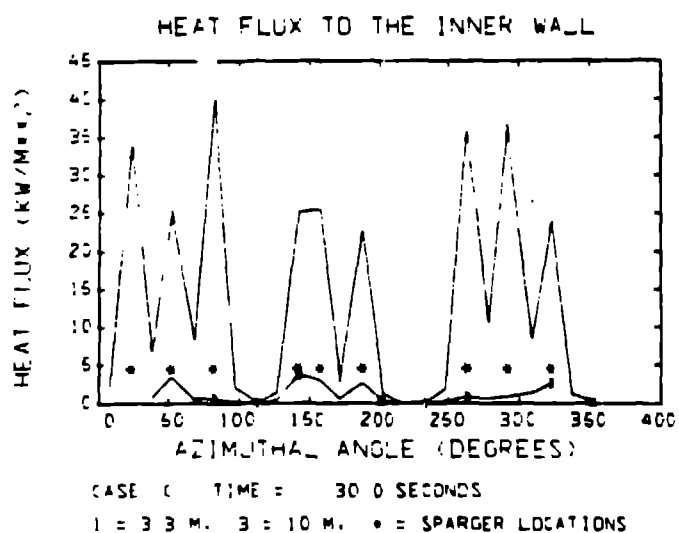


FIG. 24a Heat Flux to the Wet-wall Walls as a Function of Azimuthal Position at 30 s.

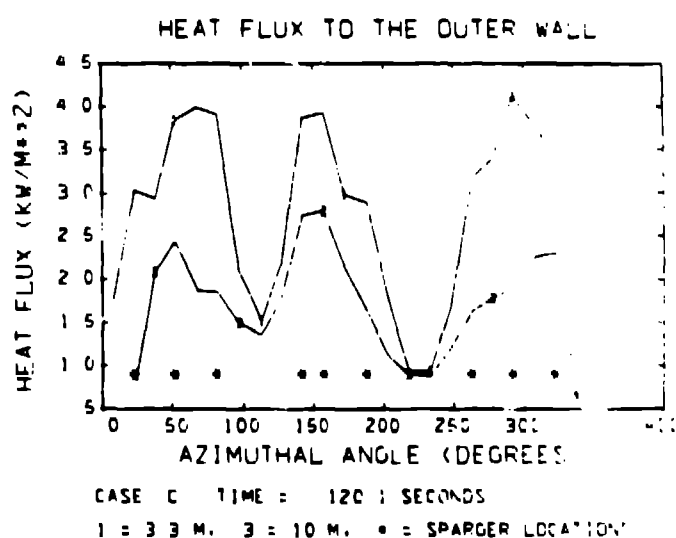
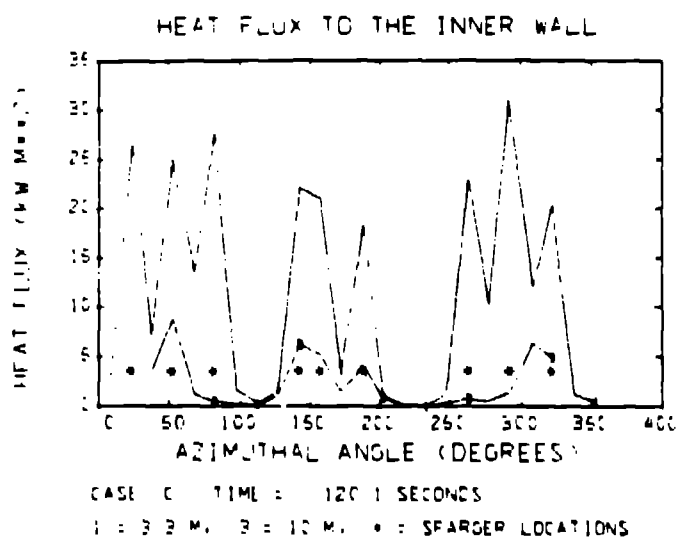


FIG. 24b Heat Flux to the Wet-wall Walls as a Function of Azimuthal Position at 120 s.

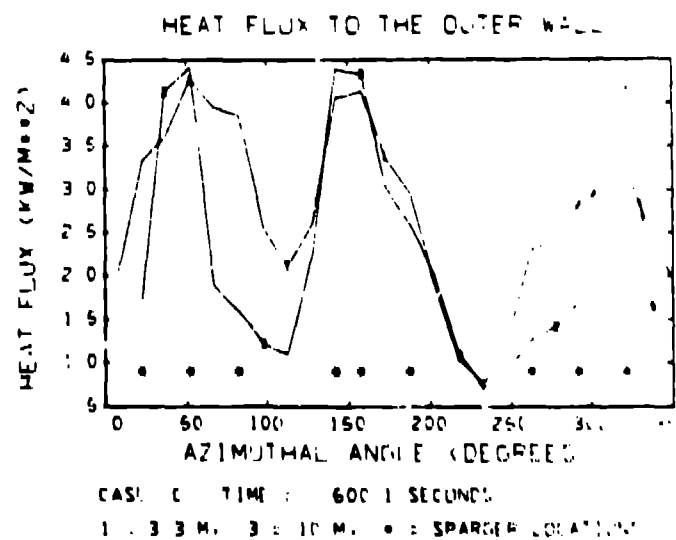
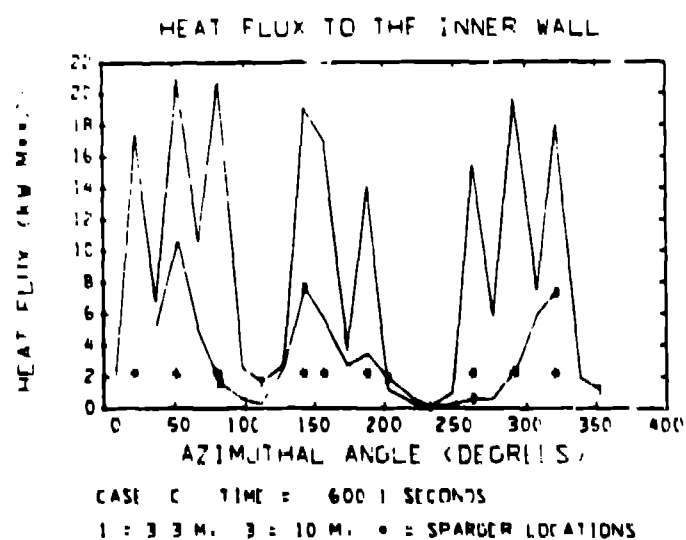
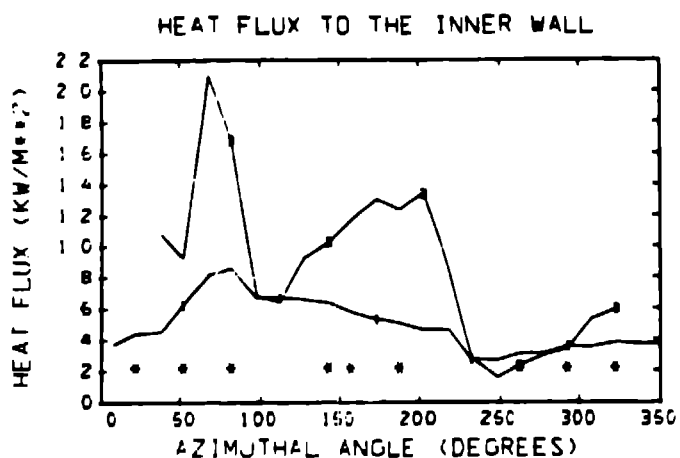
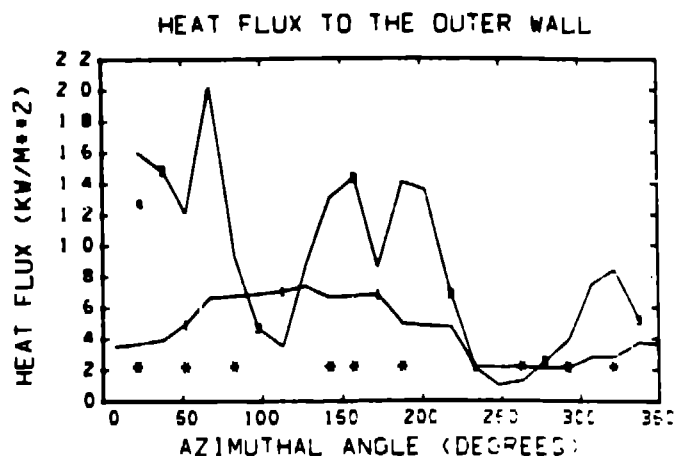


FIG. 24c Heat Flux to the Wet-wall Walls as a Function of Azimuthal Position at 600 s.

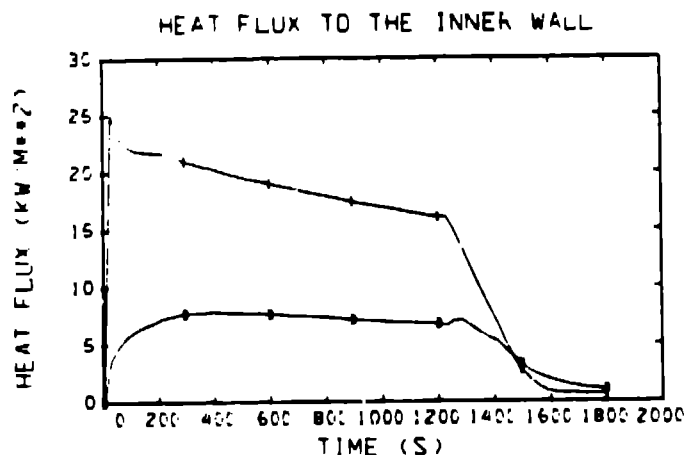


CASE C TIME = 1800.0 SECONDS
 I = 3.3 M. Z = 10 M. * = SPARGER LOCATIONS

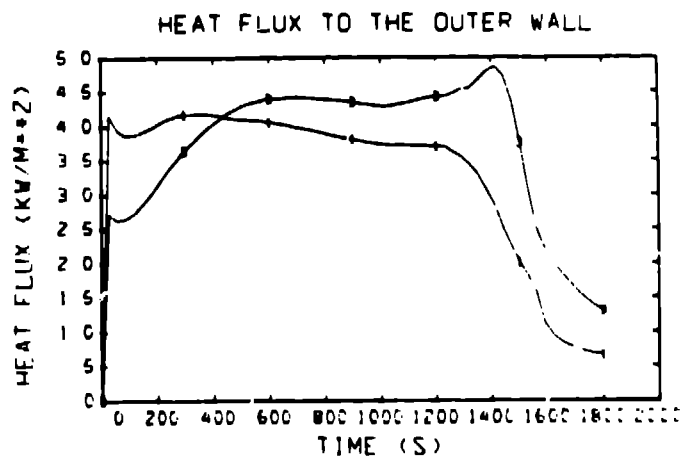


CASE C TIME = 1800.0 SECONDS
 I = 3.3 M. Z = 10 M. * = SPARGER LOCATIONS

FIG. 34d Heat Flux to the Wet-wall Walls as a Function of Azimuthal Position at 1800 s.

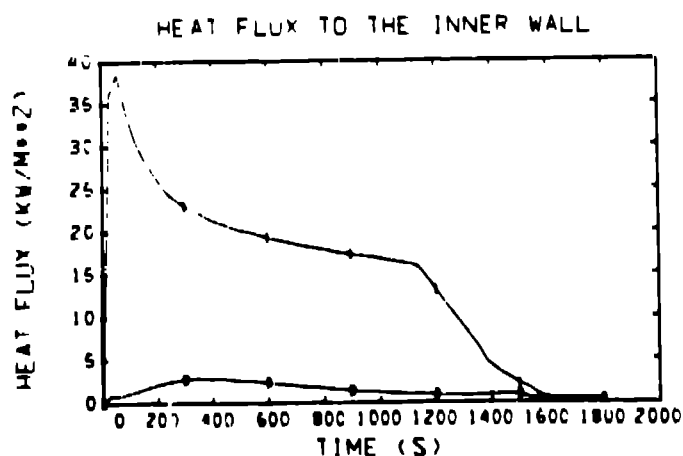


CASE C AZIMUTHAL ANGLE = 142.50 DEGREES
 I = 3.3 M. Z = 10 M

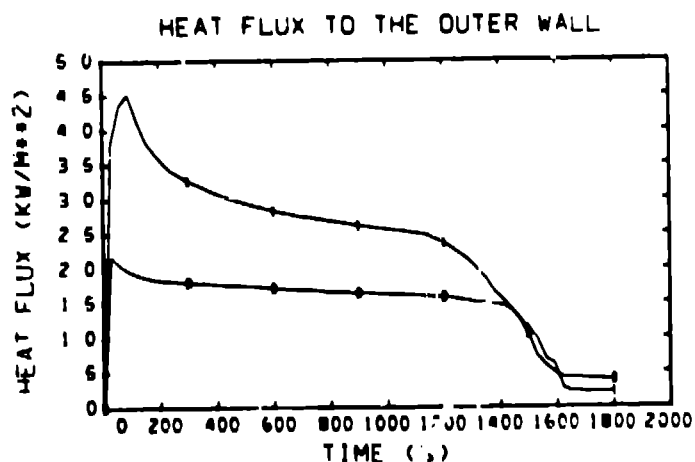


CASE C AZIMUTHAL ANGLE = 142.50 DEGREES
 I = 3.3 M. Z = 10 M

FIG. 25a Heat Flux to the Wet-wall Walls as a Function of Time at 142.5 Azimuthal Degrees.



CASE C AZIMUTHAL ANGLE = 292.50 DEGREES
 I = 3.3 M. Z = 10 M



CASE C AZIMUTHAL ANGLE = 292.50 DEGREES
 I = 3.3 M. Z = 10 M

FIG. 25b Heat Flux to the Wet-wall Walls as a Function of Time at 292.5 Azimuthal Degrees.